International Journal of Rock Mechanics & Mining Sciences 138 (2021) 104632

Contents lists available at ScienceDirect

International Journal of Rock Mechanics and Mining Sciences

journal homepage: http://www.elsevier.com/locate/ijrmms

A physical modeling-based study on the control mechanisms of Negative Poisson's ratio anchor cable on the stratified toppling deformation of anti-inclined slopes

Zhigang Tao [a], Chun Zhu [a,b,c,*], Manchao He [a], Murat Karakus [c]

[a] State Key Laboratory of Deep Rock Mechanics and Underground Engineering, China University of Mining & Technology, Beijing, 100083, China
[b] School of Earth Sciences and Engineering, Hohai University, Nanjing, 210098, China
[c] School of Civil, Environmental and Mining Engineering, The University of Adelaide, Adelaide, SA, 5005, Australia

ARTICLE INFO

Keywords:
Anti-inclined slope
Toppling deformation failure
Physical model
Deformation failure mechanism
NPR anchor cable

ABSTRACT

With ongoing increases in excavation depth, the large-scale toppling instability failure of stratified anti-inclined slopes is gaining wide attention. To address the problem of controlling toppling deformation failure of anti-inclined slopes with traditional small-deformation materials, this paper takes the results of existing studies on the extraordinary mechanical properties of engineering-scale Negative Poisson's ratio (NPR) anchor cable as a theoretical basis, and develops a model-scale NPR anchor cable according to similarity theory. Relying on a self-developed "engineering disaster model experimental system", a physical modeling-based experiment to explore the reinforcement mechanism of stratified anti-inclined slope using model-scale NPR and ordinary anchor cables is performed. The physical model is monitored using static strain data acquisition equipment, an infrared thermal imager, tension sensors, and digital speckle correlation method (DSCM) displacement field measurement equipment. The evolution of the displacement field, strain field, temperature field, and anchor cable force are obtained during excavation on the physical model. By comparing the evolution of these parameters with images from both the anti-inclined slope model instability failure test and the deformation characteristics on the two sides of the slope, which were reinforced using different types of anchor cables, this paper determines the mechanisms governing instability failure of anti-inclined slopes reinforced with NPR anchor cable. In addition, this paper also proves that NPR anchor cable can be used to monitor the sliding force of anti-inclined slopes throughout excavation, and lays a foundation for the application of NPR anchor cable monitoring technology to the advanced anti-inclined slope failure warning.

1. Introduction

Toppling failure is the primary form of failure for stratified anti-inclined slopes, which constitutes a critical scientific issue in the evaluation of anti-inclined slope stability. Stratified slopes can be classified into five types: plain-overlap slopes, consequent slopes, consequent slopes, transverse slopes, and angular slopes.[1] Obsequent slopes, also referred to as anti-inclined slopes, are rock slopes at which the strike of the strata and the slope are parallel (or intersect at a small angle) and have opposite dip. It is generally believed that because of the opposite dip between the rock strata and slope surface, anti-inclined slopes have relatively high stability, and it is difficult for them to form penetrating sliding planes or experience landslides. For this reason, anti-inclined slope deformation characteristics and evolutionary mechanisms remain largely unexplored by scholars, either domestically or globally. There is a conspicuous lack of results regarding monitoring and control methods for anti-inclined slopes.

Since the discovery of the toppling deformation phenomenon and against a backdrop of increasingly frequent engineering activities, stratified anti-inclined slopes are coming into widespread use in mining, water conservation, transportation, national defense, and other fields. Frequent engineering disturbances have successively given rise to many cases of large-scale toppling deformation failure that were previously rare occurrences.[2–5] Toppling deformation failure refers to the bending and fracturing of the upper rock mass of a slope in the free face direction (colloquially known as "nodding").[6] According to statistics, since the

* Corresponding author. State Key Laboratory of Deep Rock Mechanics and Underground Engineering, China University of Mining & Technology, Beijing, 100083, China.
E-mail address: zhuchuncumtb@163.com (C. Zhu).

https://doi.org/10.1016/j.ijrmms.2021.104632
Received 26 October 2019; Received in revised form 10 October 2020; Accepted 31 December 2020
Available online 9 January 2021

1980s, instability failure of anti-inclined slopes worldwide has caused dozens of catastrophic events with scores of casualties and a direct economic loss in the millions of dollars. Typical examples include the Jinchuan Nickel Mine in Gansu Province, Changshanhao Gold Deposit in Neimenggu province, the left-hand slope of Jinping Hydropower Station, and the north-eastern slope of the Daralou copper open pit mine[7,8]

Toppling deformation of anti-inclined slopes is the combined result of many internal and external factors, and the deformation mechanisms involved have long been a hotspot for debate.[9–14] Initially, scholars primarily used geological engineering analyses based on geological surveys to investigate field failure characteristics and failure modes as well as qualitatively summarize failure mechanisms of anti-inclined slopes. Evans[15] claimed that the reduced strength and inhomogeneous deformation of a rock mass caused by weathering, creep, stress redistribution, and other factors constituted the main secondary toppling deformation mechanisms. Teme and West[16] analyzed secondary toppling deformation instability mechanisms. Liu et al.[17] introduced a method for studying the toppling failure of anti-inclined slopes, as well as a detailed determination method for the point from bending and toppling to moving. By considering the acceleration of seismic load and joint persistence within the block base, Guo et al.[18] proposed a new analytical solution for evaluating anti-inclined slope stability under seismic loads based on the limit equilibrium method.

Scholars all over the world have taken advantage of the development of computer technology to gradually employ numerical simulations, field monitoring, and other techniques and methods to quantitatively study toppling deformation mechanisms under different working conditions. Leon-Buendia et al.[19] used universal distinct element code (UDEC) software to analyze toppling deformation mechanisms. Yang et al.[20] performed finite element simulations to explore deformation failure mechanisms of anti-inclined slopes under excavation with hard upper layers and soft lower layers. Zheng et al.[21] proposed a new UDEC Trigon approach to simulate the toppling failure of a model slope and divided the toppling deformation process into three stages. To explore the deformation and failure mechanism of an anti-inclined slope in an open pit mine, Li et al.[22] proposed a new continuum-based discrete element method for simulating the whole deformation process from continuous to discontinuous deformation.

Recently, with the development of similarity ratio theory, numerous kinds of physical modeling-based experimental systems arisen, and many scholars are now investigating topping deformation mechanisms of slopes by identifying and acquiring information regarding their internal physical fields. Majdi[23] used a tilting machine to explore deformation mechanisms of anti-inclined slopes. In 2013, Nishimura and Ueda[24,25] respectively adopted improved physical models to study this topic. Chen et al.[26] performed an experiment using a physical model to clarify the flexural toppling failure process and mechanisms in anti-inclined rock slopes. Huang et al.[27] conducted large-scale shaking table tests of anti-inclined landslides triggered by earthquakes, and studied the evolution of mechanical characteristics of soft and hard slopes under sinusoidal waves and real seismic waves, in which the failure mechanism of the Guantan landslides were obtained. In order to study the effects of seismic waves on jointed rock anti-inclined slopes, Li et al.[28] carried out shaking table experiments on anti-inclined slope models with different excitation intensities and rock types.

Due to the limitations of traditional small-deformation materials, toppling deformation failure of anti-inclined slopes characterized by large-scale deformation failure is difficult to control effectively; hence, identifying control mechanisms and key parameters for large-scale deformation constitutes a critical scientific issue for the mitigation of stratified anti-inclined slope disasters. The toppling mechanisms by which anti-inclined slopes fail are essentially different from the toppling mechanisms by which bedding slopes undergo sliding failure, meaning that many of the results generated by previous studies on slope stability cannot be used directly to either study toppling deformation mechanisms of anti-inclined slopes or evaluate stability. For this reason, due to a poor understanding of the characteristics of large-scale deformation, evolutionary mechanisms, failure mechanisms, evaluation methods, disaster-control methods, and other aspects of such slopes in engineering practice, control structures adopting traditional small-deformation materials (such as frame beams, anti-slide piles, retaining walls, and shotcrete rock bolt meshes) cannot adapt to large-scale toppling deformation in anti-inclined slopes, and ultimately fail due to instability.

Wholistic monitoring of the toppling failure of anti-inclined slopes helps to reveal failure and evolutionary mechanisms and provides early-warning information. Stability monitoring of slopes shows the laws by which slope deformation failure develops as well as sliding plane penetration mechanisms. Anti-inclined slopes are no exception in this regard, as the occurrence and development of deformation failure are manifested in a transition from quantitative change to qualitative change. After nearly 12 years of continuous field observations (2006–2018), we have summarized the whole-process landslide disasters for 12 sedimentary and metamorphic bedding slopes, from deformation through cracking, penetration, slumping, and collapse. Based on the NPR anchor cable stress evolution curve, we have discovered a scientific phenomenon of “a drop in Newtonian force and landslide occurrence,” proposed early warning modes and criteria for the long-term and tentative landslide forecasting, and successfully forecasted 12 landslide disasters.[29–33] However, flexural toppling failure of a stratified anti-inclined slope encompasses the whole process of rock mass toppling, bending, penetration, and slumping, and ultimately causes landslide disasters once fracture planes have developed and penetrated. The amount of deformation also undergoes a transition from quantitative change to qualitative change, and determines whether the anti-inclined slope will experience an overall instability failure. The mechanical characteristics and change laws of NPR anchor cable during the failure process have not been fully investigated, making acquiring the early warning modes and disaster forecast criteria even more difficult. Thus, a new technique is urgently needed to overcome the limitation of traditional small-deformation materials (i.e., tensile failure due to its failure to resist large-scale toppling deformation of anti-inclined slopes), realize a wholistic monitoring process for toppling failure, and lay a theoretical foundation for providing early warnings regarding the instability failure of anti-inclined slopes.

Relying on a self-developed “plasterboard-based experimental system to model an engineering disaster,” this paper presents a generalized geological model and performs a physical modeling-based study on stratified anti-inclined slope reinforcement using NPR anchor cables. An infrared thermal imager, strain gauges, tension sensors, and digital speckle correlation method (DSCM) displacement field measurement equipment were used to monitor the physical model and acquire data on the evolution of the displacement field, strain field, temperature field, and anchor cable force of the NPR anchor cable-reinforced physical model under excavation. Results reveal the large-deformation instability control mechanisms of anti-inclined slopes containing NPR anchor cables, and provide a reliable reference for applying NPR anchor cables to reinforcing anti-inclined slopes.

2. In-situ geological engineering investigation of the Changshanhao Gold Deposit

2.1. Geological characteristics of the Changshanhao Gold Deposit

The Changshanhao Gold Deposit is located within the Inner Mongolia province of China. The seismic zoning of the mining area is located in the North China seismic area, this area has a relatively stable geological structure. Natural earthquakes occur less frequently and at low scales within this area. The mine area has gently rolling denuded topography with low mountains and hills, with an elevation ranging 1550–1750 m. The mine area slopes form east to west, with the corresponding ore bodies primarily distributed within low-lying areas.

The primary faults are the ductile shear zone and the strike-slip

Fig. 1. Toppling failure at the real slope in the Changshanhao mine.

faults. The ductile shear zone has a NE-strike in the east, EW-strike in the middle, and NW-strike in the west, with a dip angle from 70 to 90°. The shear zone is 4.5 km long and 200 m wide and consists of several compression fracture zones and schistosized zones. Most fracture zones are distributed along-strike, with a few cutting the strata. The occurrence of fracture zones is mostly consistent with the occurrence of the rock strata. The NW strike-slip faults cross-cut the shear zones, indicating the strike-slip faults formed after the shear zones. The mine has a low rock mass integrity, and the stability of the rocks and ores are relatively poor.; therefore, during mining activities, local landslides, collapses, toppling deformation, and other geological disasters will likely occur.

The mine is located within a hilly plateau hydrogeological area, characterized by a dry climate with little precipitation and intense evaporation. The influences of rainfall and groundwater on the mine are small. A comprehensive engineering geological survey on the southwest open pit of the Changshanhao Gold Deposit was carried out. Two groups of preferred joint planes (164∠87 and 345∠84) were developed in the southwest pit, which are almost parallel to the long axis of the open pit. The two groups of joint planes have a consistent strike and opposite dip. Affected by weathering and stripping and unloading of the open pit, joint planes on the slope are have slight opening, medium ductility, high joint density, and a smooth and flat surface without filler, the joint spacing is 0.15–2 m.

2.2. Mechanism analysis of toppling deformation failure

The southwest stope of the Changshanhao Gold Deposit in Neimenggu province has already experienced several large-scale landslides of anti-inclined slopes. The highly complex rock mass structures have resulted in extremely complex deformation failure mechanisms and types. This paper takes the typical section in northern slope of the southwest stope as a case for instability mechanism analysis, and offers a basis and reference for subsequent selection of slope stability analysis and governance schemes.

According to field geological engineering surveys and geophysical exploration, deformation of north slope in the southwest stope has gone through four stages: crack development, toppling-deformation body formation, successive imbrication of toppling, and serious collapse in the lower part of the toppling failure area. The development of toppling deformation shows unique characteristics, primarily comprised of imbricate anti-inclined scarp development, hanging rock formation, platform tilting, and obvious differences in slope deformation at different locations (Fig. 1). Rock mass structures exert a fundamental control over slope deformation and failure, and soft–hard interbedded layers, anti-inclined slopes, and steeply dipping stratified structures are the defining characteristics of rock mass structures that will undergo toppling deformation failure. As indicated by geological engineering surveys of this region, the characteristics of the north slope in the southwest stope of the Changshanhao Gold Deposit meet of the above conditions, so its failure type can be defined as “toppling-deformation.”

The main stress sources for toppling deformation failure of this slope are the gravitational stress of the rock mass, the thrust of top-slumped blocks, and ground stress. These stresses, together with interbedded soft and hard layers, steeply dipping stratified rock mass structures, and loosening failure of the slope-toe-bearing stratum, constitute the basic conditions for the occurrence and development of toppling deformation failure. Seen from the perspective of deformation mechanisms, for certain rock mass structures, the loosening failure of the slope-toe-bearing stratum is a critical factor determining the occurrence and development of “toppling.” For this reason, taking targeted measures to increase the strength of the slope-toe-bearing stratum plays a significant role in preventing and controlling toppling failure of the slope.

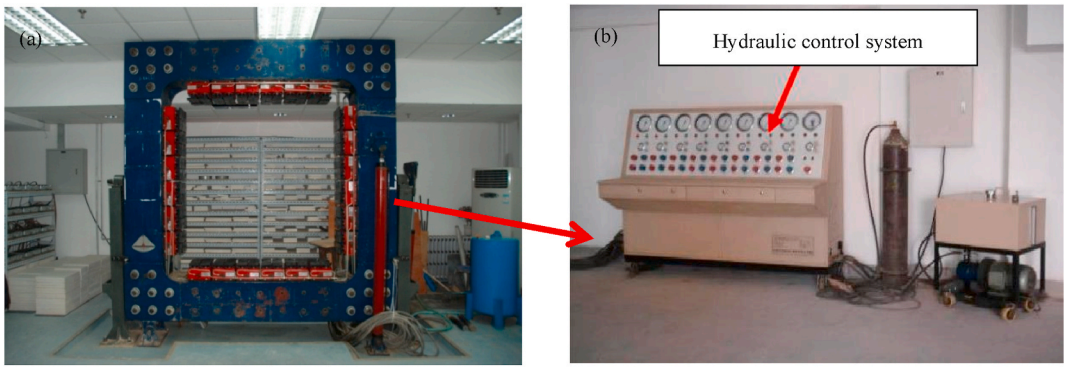

Fig. 2. Engineering disaster model experimental system: **(a)** Model experimental system; **(b)** Hydraulic control system.

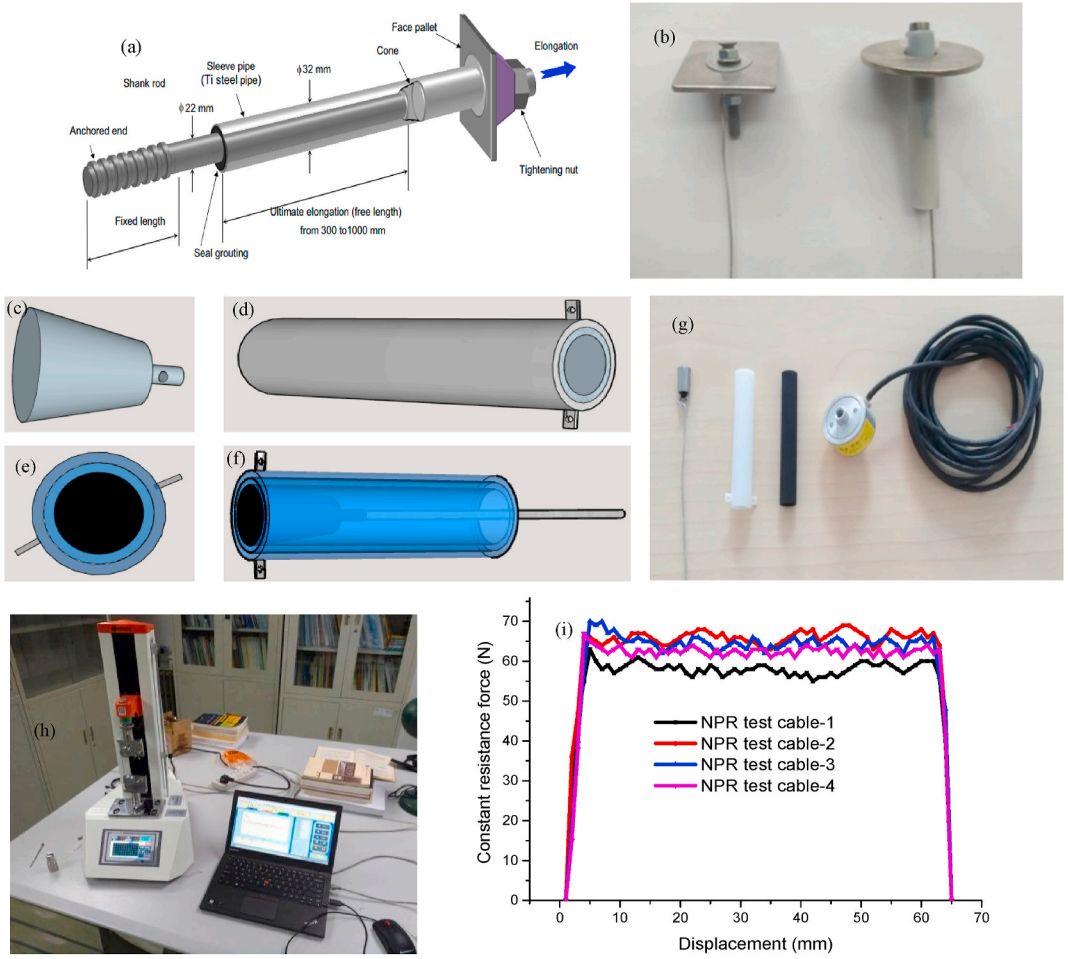

Fig. 3. Composition diagram and mechanical property test of the model-scale NPR anchor cable: (**a**) Structure of NPR cable (reference 36); (**b**) Model-scale ordinary anchor cable and NPR anchor cable; (**c**) Small constant-resistance body; (**d**) Small constant-resistance sleeve; (**e**) Front view of the constant-resistance device; (**f**) Side view of the constant-resistance device; (**g**) Physical assembly photograph of a small-scale NPR anchor cable; (**h**) Tensile test of model-scale anchor cable; (**i**) Constant resistance force curve of model-scale NPR anchor cable.

3. Physical model experimental system and development of model-scale NPR anchor cable

3.1. Physical model experimental system

Using a self-developed "engineering disaster model experimental system", this paper presents a physical modeling-based study on stratified anti-inclined slope reinforcement using NPR anchor cables according to similarity ratio theory. The experimental system consists of a support structure, a hydraulic control system, and other parts (Fig. 2) and is characterized by a nonlinear loading and a multi-purpose design.[34] The experimental system is used to apply a uniform load to the physical model.

3.2. Structure and working principle of the NPR cable

NPR cable is a kind of extendable cable with composite structure consisting of a cable body, constant-resistance body, constant-resistance sleeve pipe, pallet, and tightening nut.[36] Both the constant-resistance body and sleeve pipe constitute the constant resistance device, which can provide a constant supporting resistance for the cable (Fig. 3a).

When the slope becomes unstable, the deformation energy stored in the rock mass is slowly released, resulting in relative movement between the sliding body and the sliding bed. As the tensile force acting on cable exceeds the designed constant resistance of NPR cable, the constant-resistance body experiences friction and slippage along the constant-resistance sleeve pipe. The NPR cable can be axially extended with increasing rock deformation to slowly absorb the produced energy during slope deformation, with a maximum elongation of 2–4 m. Thus, failure induced by large deformations under conventional monitoring can be effectively avoided. Furthermore, landslides can be forecasted and estimated early using cable force monitoring curves, allowing for emergency measures to be taken to avoid danger.[32]

3.3. Similarity ratio design and material selection for the physical modeling experiment on a stratified anti-inclined slope

3.3.1. Geometric similarity ratio of the physical modeling experiment

Based on engineering geomechanics and similarity simulation, this paper introduces geomechanical simulation experimental methods and selects typical profiles to build a geomechanical model according to the geological engineering conditions in the Changshanhao Gold Deposit. Next, the physical model uses model-scale NPR and ordinary anchor cables for local slope reinforcement and explores the change laws of the surrounding rock stress field and displacement field.

The scope of the physical simulation is defined based on the principle that the initial stress state should always be maintained around the model during slope excavation. The toppling failure area of the slope selected for simulation in this experiment has a height difference of 148 m. According to the height of the original slope and considering the readjusted scope of influence of the primary rock stress field due to excavation disturbance, the prototype of the experimental simulation

Table 1
Physico-mechanical parameters of the field rock mass and expected simulation materials.

Lithology	Uniaxial compressive strength/ MPa	Elastic modulus/ GPa	Poisson's ratio	Cohesion c/ MPa	Internal friction angle ϕ/°	Density/ kg*m^{-3}
Andalusite schist	102.6	26.9	0.17	9.8	57.4	2810
Expected simulated rock mass	0.36	0.094	0.17	0.034	57.4	1870

Table 2
Physico-mechanical parameters of the prepared simulated rock mass.

Lithology	Uniaxial compressive strength/ MPa	Elastic modulus/ GPa	Poisson's ratio	Cohesion c/ MPa	Internal friction angle ϕ/°	Density/ kg*m^{-3}
Prepared simulated rock mass	0.35	0.103	0.16	0.53	21.6	1920

area is generalized to be 76 m in width (east–west), 304 m in length (south–north), and 275.5 m in height, with a slope angle of 36°. Based on the experimental equipment size, the model's geometric similarity ratio C_l is set to 190. Given that the unit weight, compressive strength, elastic modulus, and other parameters of the slope rocks in the study area are relatively high, this paper sets the unit weight similarity ratio C_r to 1.5. The other similarity constants of the simulation materials are derived according to similarity theory:

$$\begin{aligned} &C_{\sigma=}C_{E=}C_{c=}C_{\delta=}C_r{}^*C_{l=}285 \\ &C_{\mu=}C_{\varepsilon=}C_{\phi=}1 \end{aligned} \quad (1)$$

where $C_\sigma, C_E, C_c, C_\delta, C_\mu, C_\varepsilon$, and C_ϕ represent the similarity constants for stress, deformation modulus, cohesive force, displacement, Poisson's ratio, strain, and internal friction angle, respectively.

As determined from the slope rock mass distribution characteristics in the field, the rock mass of this slope segment is dominated by andalusite schist; hence, the model is primarily composed of andalusite schist. Fractures in the rock mass are under-developed, and there is a low degree of weathering in the section under investigation; therefore, the model experiment selects the main physico-mechanical parameters of rock mass and its similar materials according to model generalization and similarity constant derivation (Table 1).

3.3.2. Similarity ratio design and material selection for the physical model experiment

Through analyzing and summarizing the study results of scholars both at home and abroad regarding similar simulations, this paper selects blanc fixe (aggregate), sand (aggregate), plaster powder (cementing agent), and water (mixing agent) as the rock simulation materials.

By conducting physico-mechanical property tests on a large number of simulation materials with different proportions, this study ultimately identified simulation material proportions that satisfactorily simulate the primary rock (Table 2).

3.4. Development of model-scale and experiment on NPR anchor cable static stretching properties

3.4.1. Development of model-scale NPR anchor cable

Based on constant-resistance large-deformation anchor cables,[36–39] this paper develops a model-scale NPR anchor cable that is applicable to indoor physical modeling. To ensure that the model-scale anchor cable has the extraordinary mechanical properties of engineering-scale NPR anchor cable (such as energy consumption, high constant resistance, and large deformation), the model-scale anchor cable is similarly composed of a constant-resistance casing and a constant-resistance body (Fig. 3b). The former is divided into an outer layer (hard resin) and an inner layer (elastic rubber), while the latter takes the form of a standard cone whose diameter is greater than that of the tie rod body and is slightly greater than the inner diameter of the constant-resistance sleeve. Fig. 3 shows the design structure of model-scale NPR anchor cable, which primarily consists of a resin layer, rubber layer, constant-resistance body, and steel tie rod. The resin layer is designed with a tray at the top on the outer side so that the body can be conveniently mounted and fixed on the slope.

Table 3
Physico-mechanical parameters of materials selected for engineering-scale anchor cable and model-scale NPR anchor cable.

Anchor cable material type	Tensile load/N	Diameter/mm
Engineering-scale anchor cable	1200000	30
Model-scale anchor cable	150	1.5
Aluminum wire	131	1.5

3.4.2. Preparation of model-scale NPR and ordinary anchor cables

This experiment considers mechanical similarity and geometric similarity in the adoption of supporting structures. According to the similarity determinations for the physical model, the supporting anchor bolt has a geometric similarity ratio of $C_l = 20$, which is used to calculate the length and diameter of the anchor bolt in the physical model. The anchor cable has a mechanical similarity ratio of $C_F{=}C_\rho C_l^3 = 1.0 \times 20^3$, which is used to calculate the constant resistance and tensile load of the model-scale NPR anchor cable.

To select an anchor cable that conforms to the similarity ratio and is applicable to the model, a strength test was conducted on iron, aluminum, and copper wires of different thicknesses ($\Phi = 1$ mm and $\Phi = 1.5$ mm) using a tensile testing machine that has a maximum load of 1000 N and a range of 200 mm with a tensile rate of 20 mm/min. Aluminum wire 1.5 mm in diameter was selected to simulate the field anchor cable. Table 3 provides the physico-mechanical parameters of the anchor cable prototype and simulation materials. Anchor cables were connected with a constant-resistance device and anchorage device and assembled into a model-scale ordinary anchor cable and NPR anchor cable (Fig. 3b).

3.4.3. Experiment on static stretching properties of model-scale NPR anchor cable

The tensile testing machine was used to test the constant resistance force of the model-scale NPR anchor cable at a tensile rate of 20 mm/min (Fig. 3h). The constant resistance value of the engineering-scale NPR anchor cable is generally 750 kN. According to the mechanical similarity parameters, the constant resistance value of the model-scale NPR anchor cable should be 62.5 N. The current model-scale NPR anchor cable has a constant resistance value ranging from 58 to 67 N and 6.5 cm of constant resistance deformation (Fig. 3i). The mechanical properties of the model anchor cable are consistent with the constant-resistance mechanical properties of engineering-scale NPR anchor cable.

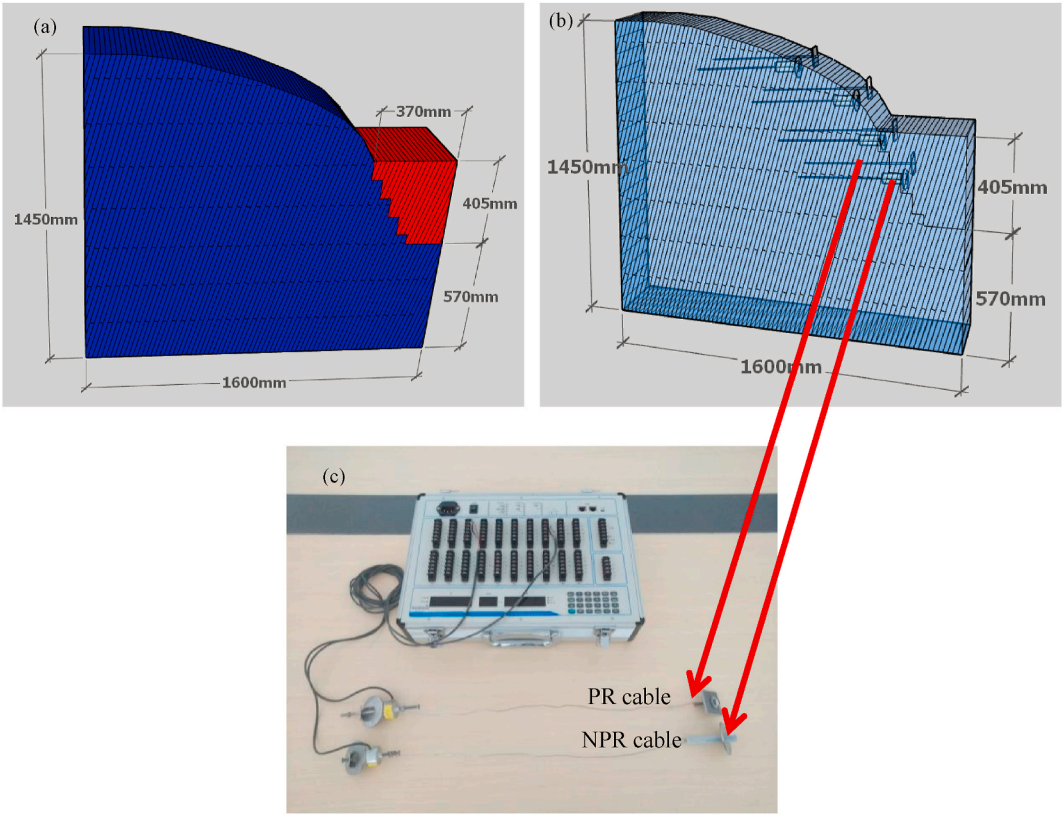

Fig. 4. Physical model-building for the anti-inclined slope after anchor cable reinforcement: (**a**) Schematic diagram of the anti-inclined slope model; (**b**) Schematic layout of model-scale NPR anchor cables in slope model; (**c**) Photographs of model-scale anchor cable.

4. Physical modeling experiment on the controlling effect of NPR anchor cable on toppling failure of an anti-inclined slope

The physical model experiment was set up with the previously described slope segment based on the Changshanhao Gold Deposit in Neimenggu province. Model-scale NPR and ordinary anchor cables were buried on either side of the slope for the purpose of exploring variations in the stress and strain fields of a slope rock mass under excavation after reinforcement with different types of anchor cables.

4.1. Physical model-building for the anti-inclined slope after anchor cable reinforcement

4.1.1. Generalized geological model-building for the anti-inclined slope and layout of model-scale NPR anchor cables

A slope model was built with a 75° rock strata angle, as well as length, width, and height dimensions of 160 cm, 40 cm, and 145 cm, respectively. The excavation area is located at the slope toe and is excavated in nine successive layers, each with an excavation depth of 4.5 cm. The excavation area has an overall length of 37 cm and a depth of 40.5 cm (Fig. 4a).

The area considered susceptible to instability according to existing modeling experiments (Fig. 5) and field data was reinforced with anchor cables.[40] To explore the control provided to an anti-inclined slope by NPR and ordinary anchor cables respectively, model-scale NPR anchor cables were buried on the outer side of the slope model, while model-scale ordinary anchor cables were buried on the inner side. Through comparing the controlling effects of the different anchor cables, this paper investigates the instability failure control mechanisms of NPR anchor cables on anti-inclined slopes.

Based on the density of field anchor cable reinforcement and the size of the physical model, four sites on the model slope were selected at which a total of eight anchor cables were mounted (Fig. 4b). The four anchor cables in the excavation area were buried before excavation, and they were installed and pre-tightened after excavation. Model-scale NPR anchor cables were first made according to the predesigned size, and anchor cable mechanical properties were then tested; after achieving the intended effects, they were connected to tension sensors. The installation of model-scale anchor cable adopted the pre-embedding method, and the tension sensor was arranged inside the model to explore stress variations of the model-scale anchor cables during slope excavation. During the construction process, the plasterboards were drilled to embed the anchor cable, so that the anchor cable passed through the plasterboard and then was fixed in the predetermined position of the model. Because there is no need to drill holes for installing the anchor cables during the experiment, and the disturbing force of installation is relatively small, thus the performance of individual bolt is not affected by another bolt installation. The small-scale anchor cables for physical model experiment are shown in Fig. 4c.

4.1.2. Strain gauge layout

To comparatively analyze the controlling effects of the two different types of anchor cables on instability failure of the anti-inclined slope, two rows of strain gauges were arranged symmetrically on either side inside the rock slope model to identify variations in the strain field when reinforced using different anchor cables. Strain gauge monitoring planes are located at cross sections at 100 mm and 300 mm in the Z direction inside the model. Each row in the physical model has 40 strain gauges (80 in total). The number of strain gauges of each row in the excavation area on the right-hand side of the slope increases appropriately, especially in the slope toe (Fig. 6). Strain monitoring segments are divided into layers 1–6 from the top to the bottom of the slope, and the strain gauges are numbered in increasing order from right to left.

A three-dimensional 45° strain gauge was used to measure the strain

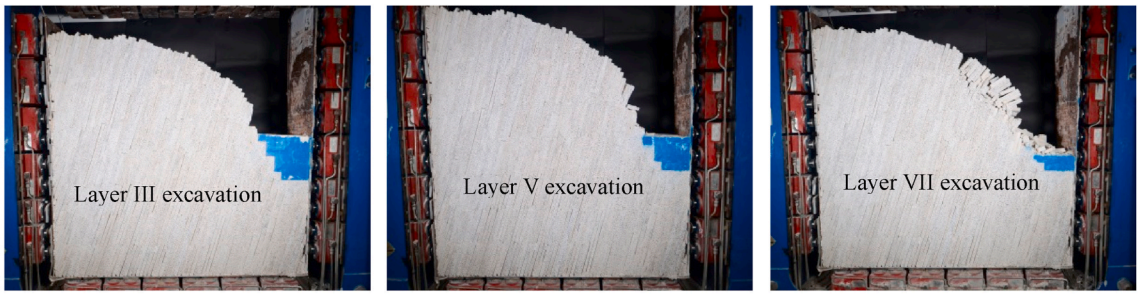

(a) Deformation characteristics of slope model during excavation

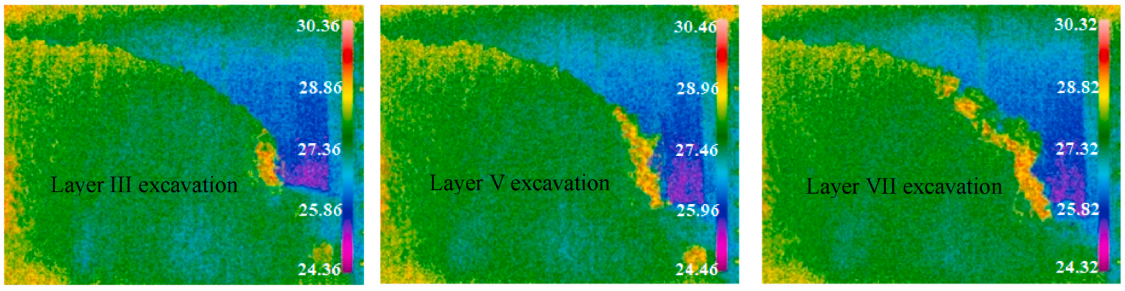

(b) Infrared temperature distribution characteristics of slope model during excavation

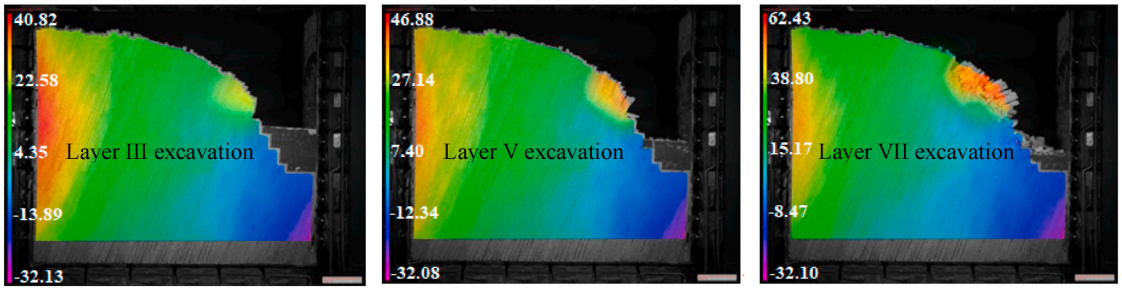

(c) Horizontal displacement distribution characteristics of slope model during excavation

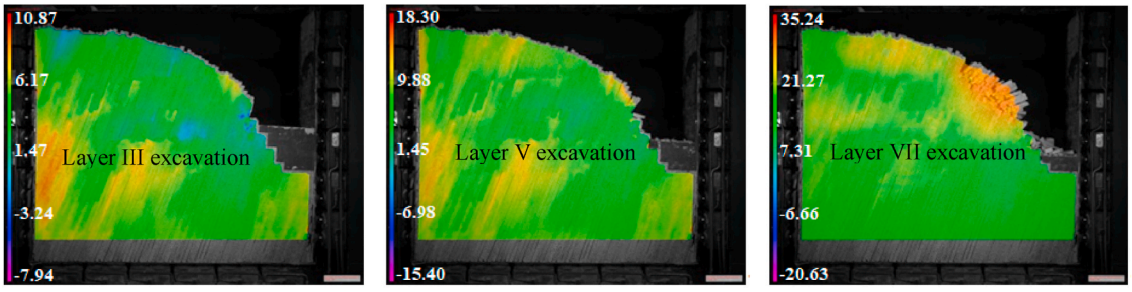

(d) Vertical displacement distribution characteristics of slope model during excavation

Fig. 5. Instability failure characteristics of an anti-inclined slope model during excavation (reference 40).

values inside the slope. Grooves were excavated beside preset sites on the plates, strain gauges were pasted in the grooves, and the layout of the strain gauge monitoring points was realized through the placement of these plasterboards to which the strain gauges were attached.

After processing and analyzing the data from the monitoring points in three directions, the maximum principal strain value of each monitoring point was calculated using Eq. (2).

$$\varepsilon_{max} = \frac{1}{2}\left[(\varepsilon_x + \varepsilon_y) + \sqrt{2\left[(\varepsilon_x - \varepsilon_u)^2 + (\varepsilon_u - \varepsilon_y)^2\right]}\right] \quad (2)$$

where ε_{max} is the maximum principal strain; ε_x, ε_u, and ε_y are the measured strains in the directions of X, U, and Y, respectively (Fig. 6c).

4.1.3. Loading design

The first step in the experiment was to apply a horizontal load of P = 0.2 MPa to each side of the model in order to obtain a degree of compaction similar to that in the field. After 10 min of pre-compaction, the horizontal confining pressure was held constant at 0.2 MPa, and the slope was excavated layer by layer (Fig. 6d).

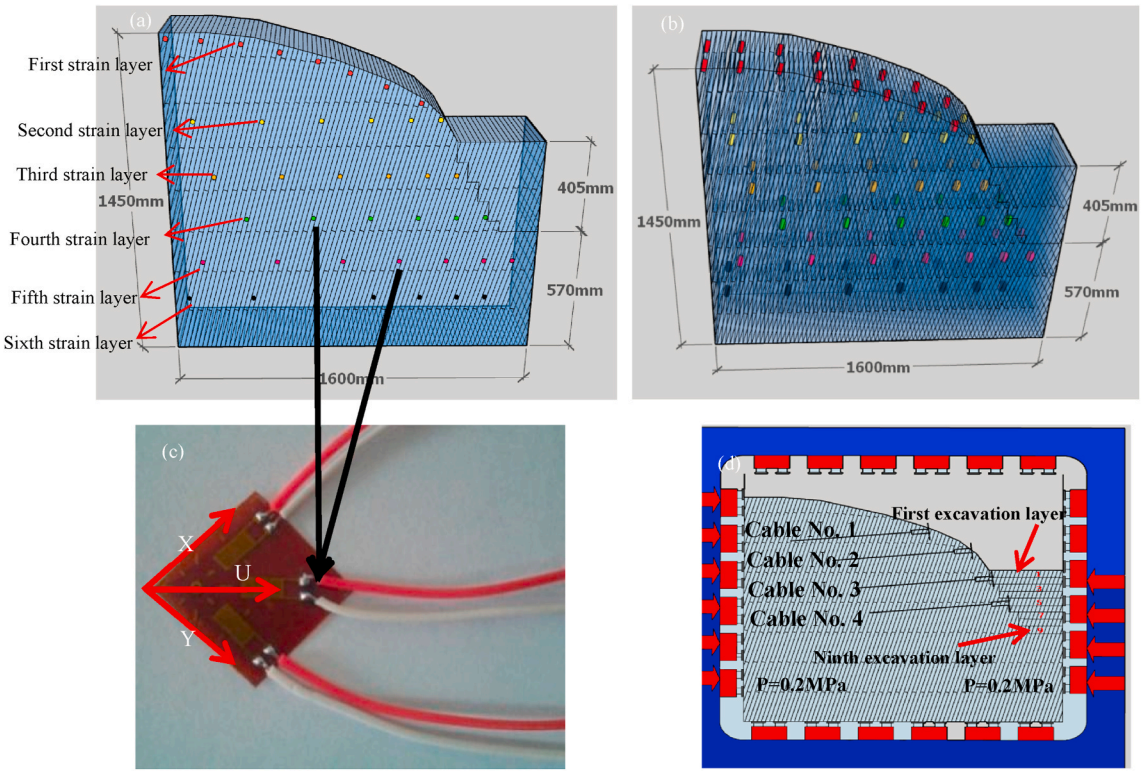

Fig. 6. Schematic layout of strain gauges and cables inside the slope: (**a**) Front view of strain gauges inside slope; (**b**) Three dimensional view of strain gauges inside slope; (**c**) Three-dimensional 45° strain gauge; (**d**) Cable layout and experiment process of slope model.

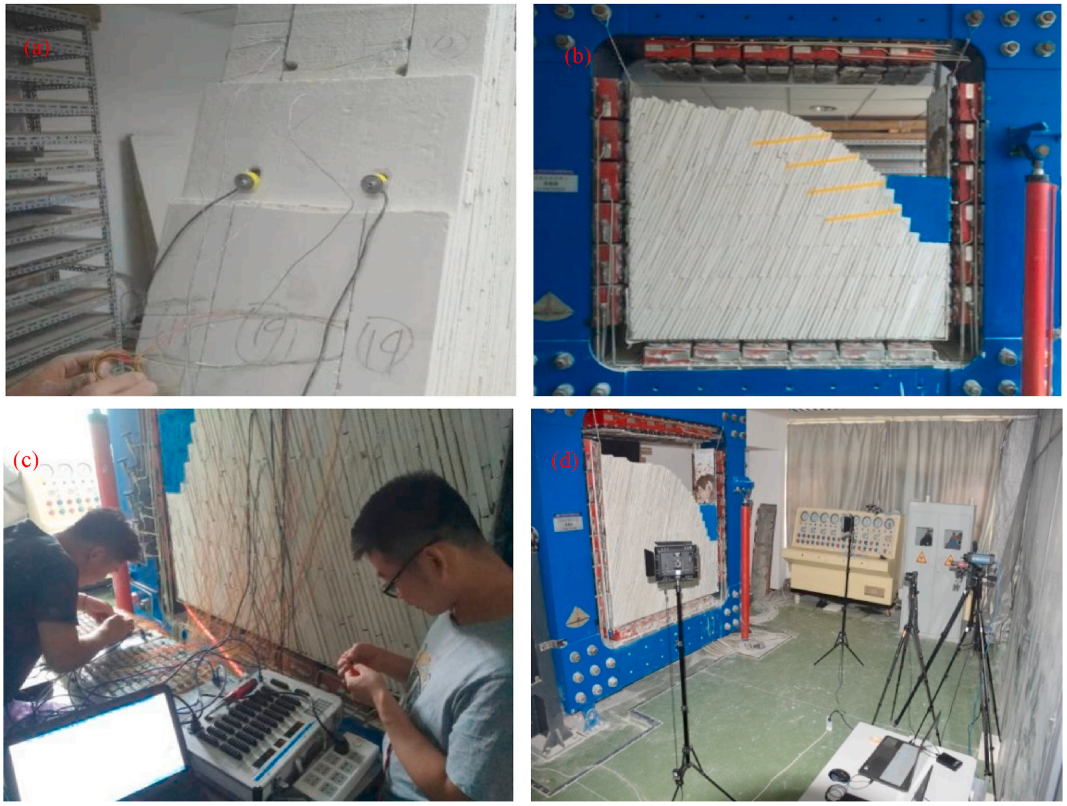

Fig. 7. Main steps in the construction of the physical model experiment: (**a**) Layout of strain monitoring points and tension sensors; (**b**) Completed the model; (**c**) Connection of monitoring equipment wires; (**d**) Layout of digital image acquisition equipment.

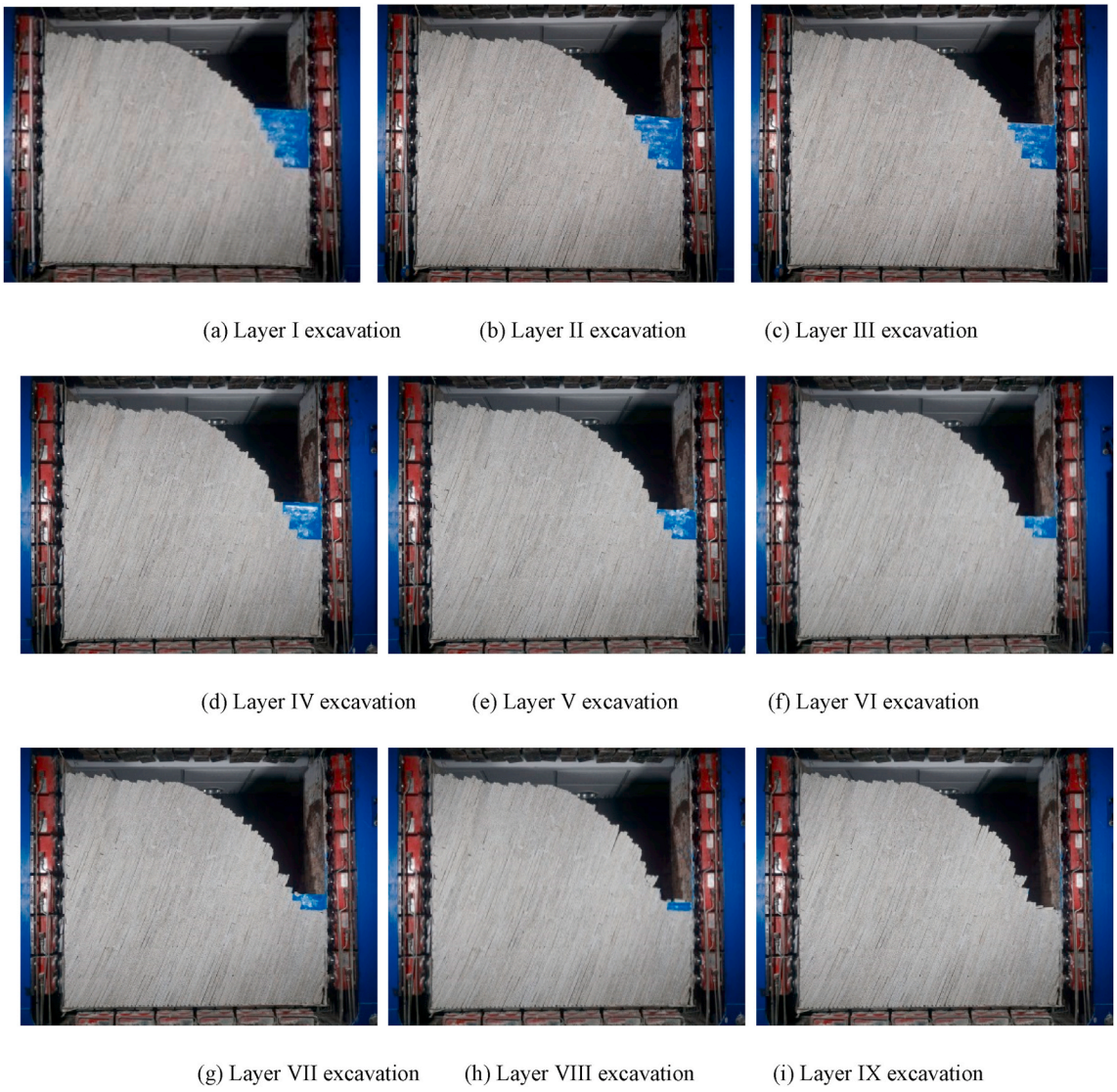

Fig. 8. Deformation of anti-inclined slope reinforced by anchor cable under excavation.

4.1.4. Comprehensive equipment for monitoring various mechanical fields in the physical modeling experiment

The physical model employed static strain data acquisition equipment, an infrared thermal imager, tension sensors, and DSCM displacement field measurement equipment to detect changes in the stress field, displacement field, temperature field, and anchor cable force. The strain data acquisition equipment used was a YSV8360 static strain tester, which has a range of ±20,000 με, a resolution of 5 με, and a maximum sampling frequency of 5 Hz. During the experiment, there was stress redistribution inside the rock mass due to slope unloading, which further caused the slope to release energy through slow deformation. An infrared thermal imager can accurately capture the area being deformed in the slope and avoid the influence of contact measurement on the experimental model. The DSCM displacement field measuring system was used to measure the displacement of the model slope based on the movement of artificial speckles applied to the model's surface. By matching the geometric positions of speckles on the rock surface in digital images taken over time, the movement traces can be used to characterize the deformation.

4.1.5. Geometric-physical model-building

Plasterboards were prepared according to the previously designed similar simulation material proportioning. To simulate the current status of the anti-inclined slope at the Changshanhao Gold Deposit, plasterboards were used to build a slope model based on the 36° anti-inclined rock slope. To appropriately simulate the stratification of the real strata, plaster plates of two specifications (40 cm × 40 cm × 2 cm and 40 cm × 20 cm × 2 cm) were stacked alternately during model building. Because the in-situ rock mass is alternating layers of slate and schist with no filler between layers, the shear strength of the joints delimiting the rock slates can be ignored in the model. Rock joints are distributed along the contact surfaces between slates. Plasterboards are stacked directly without adding any bonding material, and a horizontal stress was applied on both sides of the model to compact the model before excavation. Joint inclination is 75°, and joint spacing is 2 cm. Using the joint strength test, the internal joint friction angle in the model is determined to be 19°. Therefore, plasterboards are used to structure the model, and the fissures between plasterboards can truly reflect the in-situ characteristics of rock joints to some extent. The layout of strain gauge monitoring points and model-scale anchor cables was realized through the placement of plates, and strain gauge wires and tension sensor wires were connected to a static strain tester. After speckles had been drawn on the side of the model, the position of the monitoring equipment was adjusted to capture the model deformation (Fig. 7).

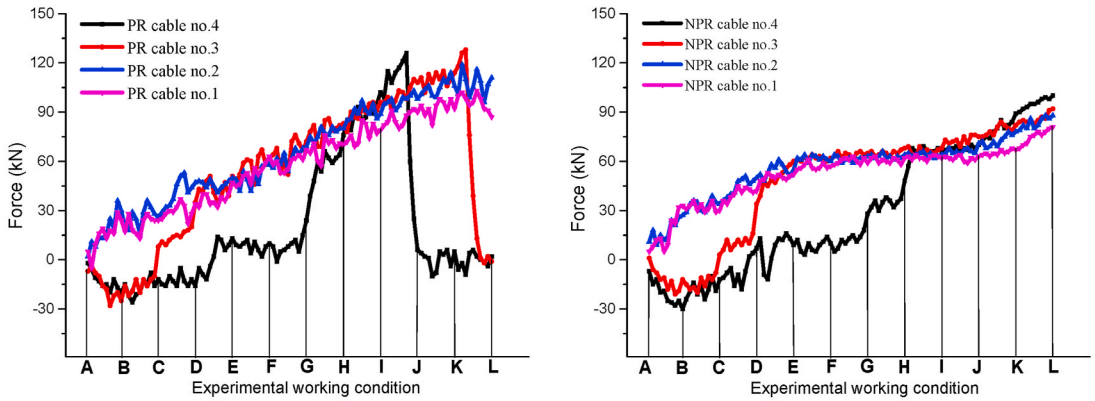

Experimental wording condition: A——Start loading; B——After loading; C——After excavation of first layer; D——After excavation of second layer; E——After excavation of third layer; F——After excavation of fourth layer; G——After excavation of fifth layer; H——After excavation of sixth layer; I——After excavation of seventh layer ; J——After excavation of eighth layer; K——After excavation of ninth layer; L——Test finish.

(a) The axial force of model-scale anchor cables (PR cables and NPR cables)

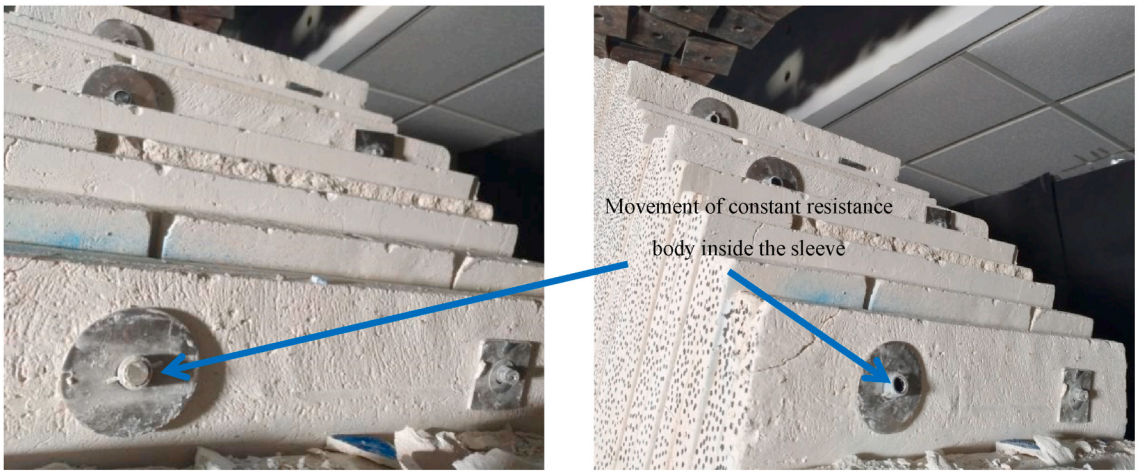

(b) Tension-comparsion photographs of model-scale NPR anchor cable

Fig. 9. Evolution characteristics of the axial force and deformation of model-scale anchor cables.

4.2. Physical model experiment

First a horizontal load of P = 0.2 MPa was applied on each side of the model with an experimental machine to fully compact the strata. After loading was completed, the slope was excavated layer by layer according to the designed mining path until the designated limit had been reached. The static strain data acquisition equipment, infrared thermal imager, tension sensor, and DSCM displacement field measurement equipment were used to capture information on the deformation failure of the model slope throughout the experiment.

Each layer was excavated at a depth of 4.5 cm, and after the excavation of one layer, the slope was allowed to stabilize for 1 h before the next layer was excavated. There were nine layers in total. Fig. 8 shows the deformation status of the surrounding rock of the slope during excavation.

4.3. Analysis of monitoring results

This paper uses all of the data acquired from the monitoring equipment to assess the model slope deformation and determine the characteristics and change in the displacement field, strain field, temperature field, and anchor cable force of the NPR anchor cable-reinforced model slope.

4.3.1. Stress condition of anchor cables during excavation

Tension sensors were used to measure the axial force vs. time of the model-scale NPR and ordinary anchor cables (Fig. 9a). Anchor cables NPR1–NPR4 on the outer side are NPR anchor bolts, and anchor cables PR1–PR4 on the inner side are ordinary anchor bolts. In the loading stage, the axial force monitoring curves of anchor cables No. 1 and No. 2 on both sides increase continuously; however, anchor cables No. 3 and No. 4 on both sides are still buried in the slope and in an extrusion state, producing a negative axial force. After excavating layer I, the axial force on anchor cable No. 3 on both sides begins to rise, and the axial force on both No. 4 anchor cables begin to rise after excavating layer V.

Overall, the anchor cable monitoring curves increase at a slower rate during the early excavation stages compare to the loading stage. In the middle stage of excavation, the NPR anchor cable monitoring curve remains steady at a constant resistance of 60–66 N, while that of ordinary anchor cable increases continuously. During late stage excavation, sometime after layer VII excavation, the axial force on the ordinary anchor cable No. 4 drops abruptly after reaching its peak, suggesting that the stress has exceeded the anchor cable bearing capacity, and the cable has broken due to the deformation of the slope. Sometime after the completion of layer IX excavation, the axial force on ordinary anchor cable No. 3 drops abruptly, suggesting that this ordinary anchor cable also failed during slope unloading. In contrast, the axial forces on anchor

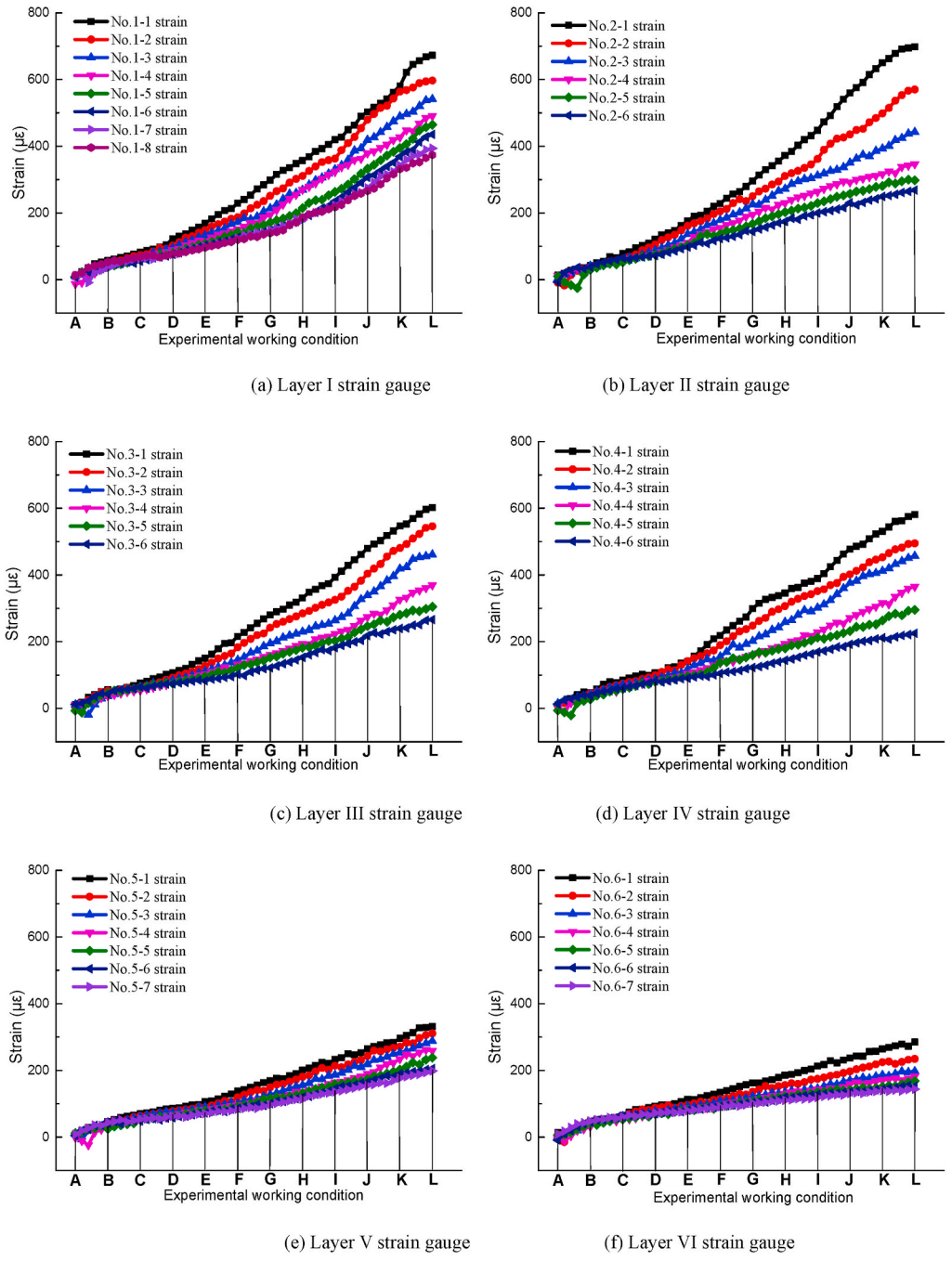

Experimental wording condition: A——Start loading; B——After loading; C——After excavation of first layer; D——After excavation of second layer; E——After excavation of third layer; F——After excavation of fourth layer; G——After excavation of fifth layer; H——After excavation of sixth layer; I——After excavation of seventh layer ; J——After excavation of eighth layer; K——After excavation of ninth layer; L——Test finish.

Fig. 10. Strain gauge monitoring curves for the ordinary anchor cable-reinforced side of the physical model.

bolts NPR1–NPR4 remain in a slow growth state until excavation is completed and monitoring stops. To be specific, the maximum axial forces on anchor bolts NPR1–NPR4 are respectively 80 N, 88 N, 91 N, and 99 N, all of which are far lower than the maximum tensile stress of the anchor cable material.

The slope toe has the highest degree of deformation failure, and the two ordinary anchor cables on the inner side at the slope toe fail as a result of overloading. The two ordinary anchor bolts at top of the slope bear relatively low stresses, and their axial forces do not exceed their maximum tensile loads (maximum loads: 107 N and 91 N). In contrast, no NPR anchor cable failed, and all of them record a slow increase in tension with a large slope deformation. Under tensile stress, the constant-resistance body moves in the constant-resistance sleeve (Fig. 9b). The amounts of deformation on NPR anchor cables No. 1, No. 2, No. 3, and No. 4 were 0.8 cm, 1.2 cm, 2.6 cm, and 3.1 cm, respectively, proving that NPR anchor cable can fully accommodate a relatively large amount of deformation during slope excavation, forcing the rock mass into a secondary equilibrium state. In addition, NPR anchor

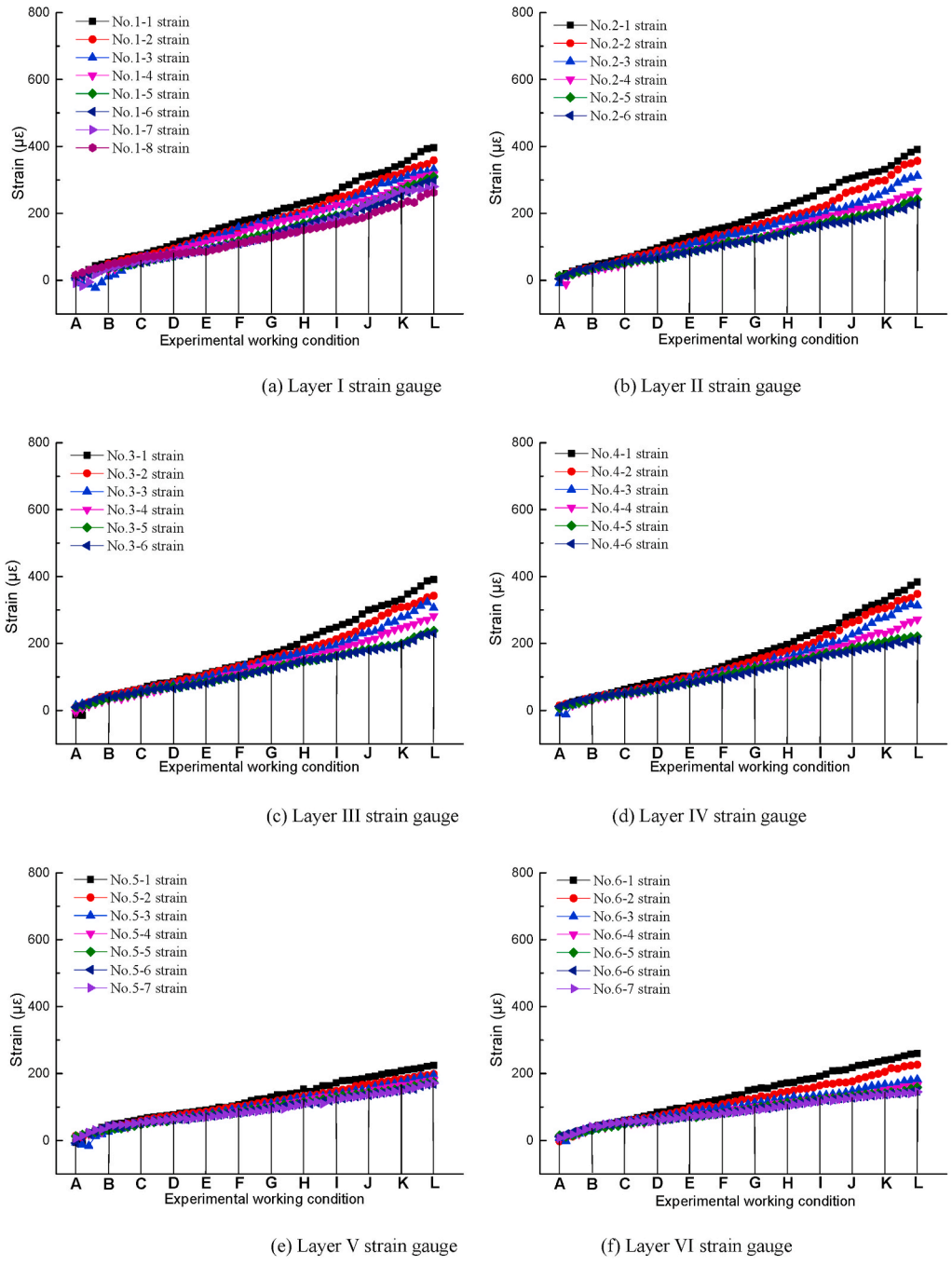

Experimental wording condition: A——Start loading; B——After loading; C——After excavation of first layer; D——After excavation of second layer; E——After excavation of third layer; F——After excavation of fourth layer; G——After excavation of fifth layer; H——After excavation of sixth layer; I——After excavation of seventh layer ; J——After excavation of eighth layer; K——After excavation of ninth layer; L——Test finish.

Fig. 11. Strain gauge monitoring curves for the NPR anchor cable-reinforced side of the physical model.

cables can be used to monitor the sliding force of an anti-inclined slope throughout excavation and provide an early instability failure warning for anti-inclined slopes during excavation.

4.3.2. *Internal strain field evolution in the physical slope model*

This study measured the maximum principal strain value at each monitoring point using strain gauges arranged symmetrically on both sides of the model, plotted the resulting strain monitoring curves, and obtained the internal stress field change laws on both sides of the slope model after reinforcement using different anchor cable types. Strain curves for the slope model with ordinary anchor cable reinforced-sides are shown in Fig. 10, and those for NPR anchor cable-reinforced sides are shown in Fig. 11.

Strain gauges in layers 5 and 6 were located below the excavation area; hence, their strain values changed at relatively low amplitudes and showed similar trends with relatively small strains. The strain gauges in layers 2–4 were arranged horizontally; those close to the slope surface were greatly influenced by excavation, while those inside the slope and

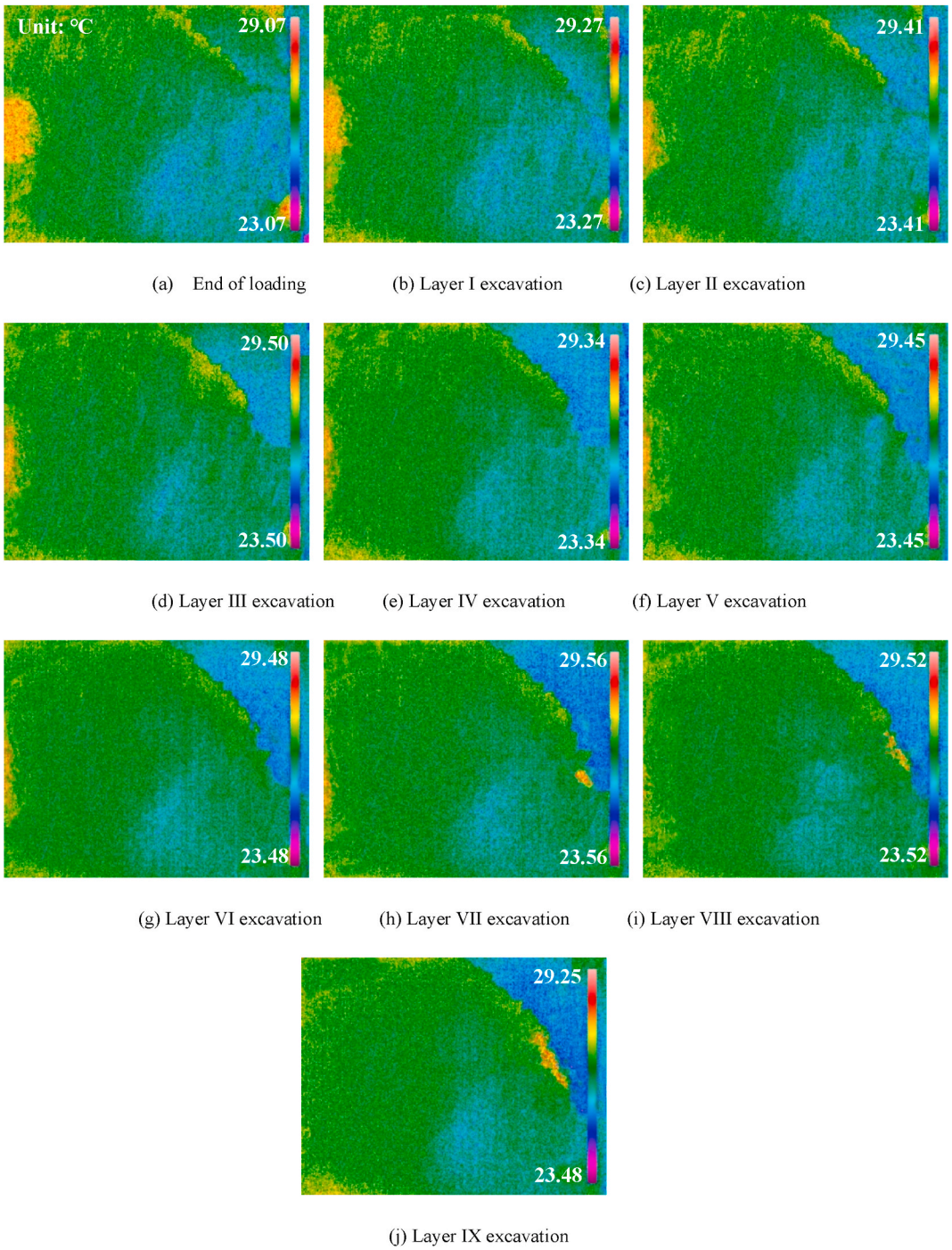

Fig. 12. Infrared temperature images of the physical model.

far away from the excavation face were influenced to a much smaller extent. Layer 1 strain gauges were arranged along the slope top, and the strain gauges in this layer recorded significant strain variations relative to those in other layers. After the excavation of layers VII and IX, ordinary anchor cables No. 4 and No. 3 on the inner side of the slope successively failed due to overloading, giving rise to a local collapse of the rock mass. As a result, the monitoring points close to the collapse area in layers 3 and 4 saw abruptly strain increases. The ordinary anchor cable-reinforced side strain values increased significantly, and the strain values of the NPR anchor cable-reinforced side were also affected, as illustrated by the slight increase in the slope of the curves (Fig. 11).

Comparing Figs. 10 and 11 indicates that in the early stages of slope excavation, the amplitudes of change in the internal strain values on the NPR anchor cable-reinforced side are similar to those on ordinary anchor cable-reinforced side. With continuous slope excavation, there was a decline in the amplitude of change in the internal strain values on the NPR anchor cable-reinforced side. This is primarily because although the unloading of the rock mass caused the slope to gradually deform, NPR anchor cable can absorb the energy produced by the slow deformation, maintain constant resistance, accommodate a large amount of deformation, maintain the stability of the slope rock mass, and force the rock mass into a secondary equilibrium state. No NPR anchor cables failed throughout the entire excavation process. Overall, the strain curves for the NPR anchor cable side of the slope all recorded relatively steady growth. Strain values varied in relatively narrow ranges in all layers except layers 3 and 4 (in which the strain gauges saw slight

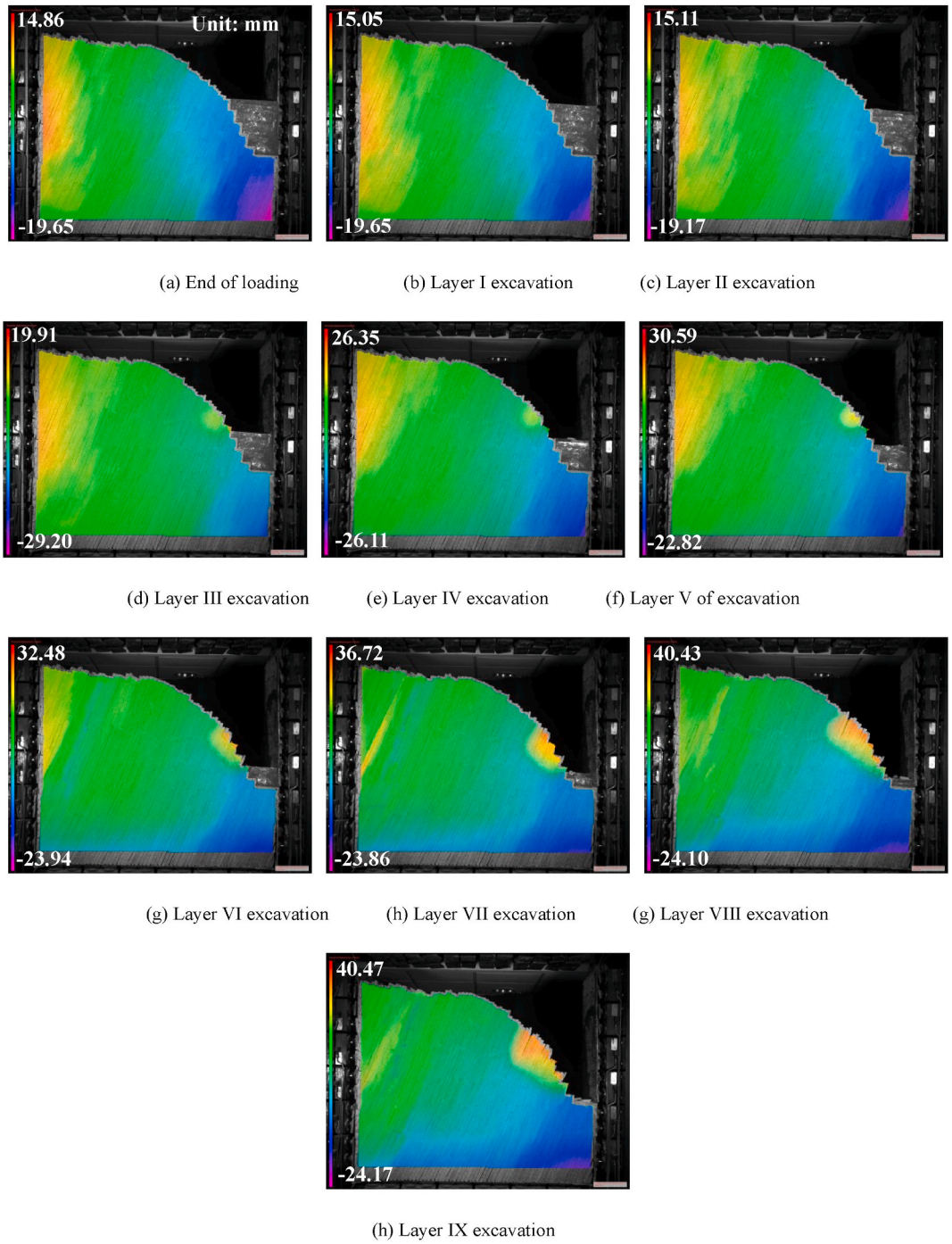

Fig. 13. Horizontal displacement nephograms of the physical model.

sudden increases in strain values in the late stage of excavation).

4.3.3. Internal temperature field of the physical slope model

An infrared thermal imager was used to measure the temperature of the reinforced anti-inclined slope model throughout excavation. Nephograms representing the temperature field of the physical model are shown in Fig. 12.

After loading of the slope model, the temperature rose on both sides of the model, and the temperature in the central area on the left side reached 27.7 °C (Fig. 12). During slope excavation, with the continuous release of energy on both sides of the model, the temperature eventually dropped to room temperature. Reinforced by anchor cables, the slope had relatively high overall stability, except in the late stage of slope excavation (in which local collapse took place on the inner side of the slope model). For this reason, during the late stage of excavation, the temperature nephogram shows a rise in local temperature in the excavated area of the slope, while temperatures in other areas are relatively stable, indicating that temperature can be used accurately judge the distribution of unstable deformation within the slope and lay a foundation for a rational reinforcement scheme.

4.3.4. Internal displacement field of the physical slope model

A CCD camera was used to take pictures throughout the experimental process, and the displacement fields of the slope at different moments were obtained from the collected images. However, given that the camera was placed on the side reinforced by NPR anchor cables, the

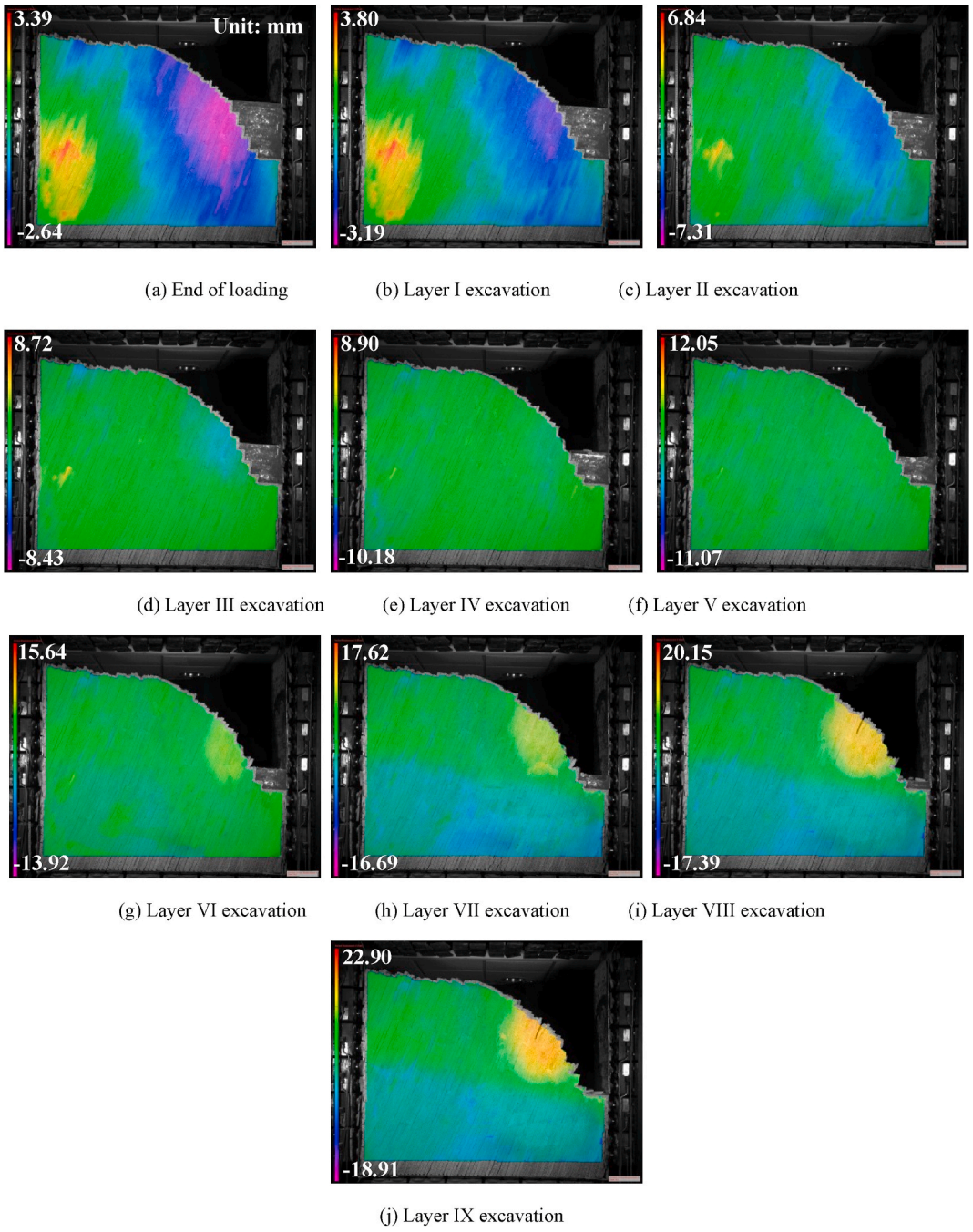

Fig. 14. Vertical displacement nephograms of the physical model.

displacement nephogram only shows the evolution of slope displacement on that side (Fig. 13 and Fig. 14).

(1) Horizontal displacement nephograms of the physical model (Fig. 13):

The system sets rightward displacement as the default positive direction and leftward displacement as the negative direction. After slope loading, the displacements on the two sides of the slope model were relatively large. To be specific, the left side had a maximum deformation of 11.81 mm, while the right side had a maximum deformation of 15.35 mm. With continued slope excavation, the free face of the slope was unloaded, which destroyed the original stress state, causing stress redistribution inside the slope. Given that the slope was reinforced on both sides with anchor cables, it had high overall stability and small displacement relative to the case without anchor cable reinforcement (Fig. 5). With continuous excavation of the slope, the rock mass experienced a slow transition from its original extrusion state to a state of tensile fracturing. Upon excavation of layer VII, ordinary anchor cable No. 4 failed, and the rock mass in this area lost support and deformed, resulting in local collapse. The NPR anchor cable side and the ordinary anchor cable side were located on the same element plate structure, so the lower area of the slope on the NPR anchor cable side also experienced a relatively large displacement. Upon excavation of layer VIII, the slope showed minor V-shaped fractures, and the amount of local maximum displacement reached 29.14 mm. In this case, fracturing occurred along the relatively weak joints between the rock mass on the ordinary anchor cable-supported side and that on NPR anchor cable-

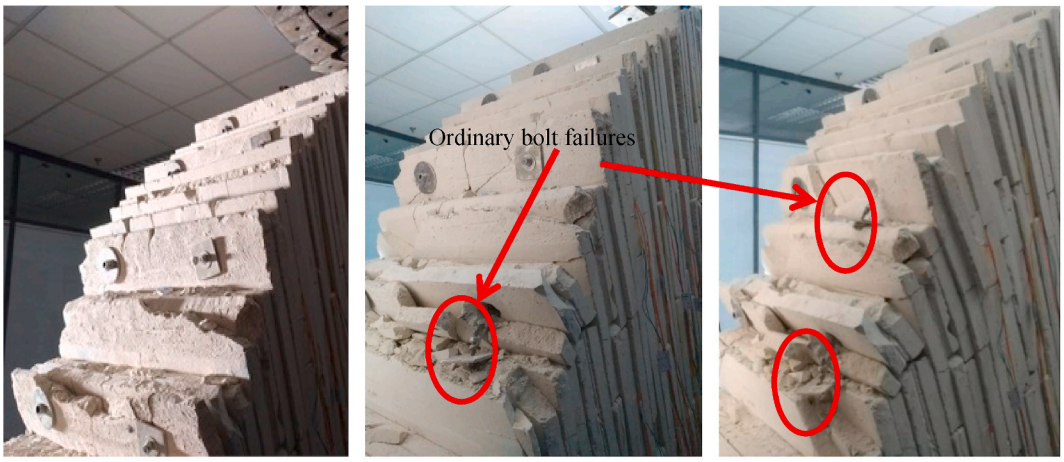

(a) Evolution of the anchor cable on each side of the slope

(b) Failure characteristics of the side of anti-inclined slope model reinforced by PR anchor cables

Fig. 15. Comparison of the sides of the anti-inclined slope model reinforced by different types of anchor cables.

supported side. At the end of excavation, V-shaped fractures propagated through the rock mass, and the local maximum displacement reached 31.96 mm; however, NPR anchor cable-supported side of the slope remained in a relatively stable state and experienced no instability failure.

(2) Vertical displacement nephograms of the physical model (Fig. 14):

The system sets downward displacement as the default positive direction and upward displacement as the negative direction. After slope reinforcement, the degree of compaction between element plates was relatively high, so the slope model had a relatively small vertical displacement during the loading process (Fig. 14). As it was extruded by loads on both sides, the anti-inclined slope model experienced an upward displacement on the left side (a maximum of 2.68 mm), and a downward displacement on the right side (a maximum of 2.15 mm). With gradual excavation of the slope, the model experienced a relatively small amount of overall deformation with an overall relatively small vertical displacement except in the late stage of excavation (in which a relatively large vertical displacement (a maximum of 17.83 mm) occurred in the vicinity of the V-shaped fracture).

5. Comparative analysis of the control effects of NPR and ordinary anchor cables for anti-inclined slopes

Under slope excavation, flexural toppling failure of a stratified anti-inclined slope goes through a process of rock mass toppling, fracturing, penetration, and slumping (Fig. 5). The development and penetration of fracture planes ultimately leads to landslide disasters, accompanied by the transition from a quantitative change to a qualitative change in the amount of deformation. A rise in overall stability was seen after reinforcing the slope model with model-scale NPR and ordinary anchor cables. In the early stage of slope excavation, ordinary anchor cables were sufficient to guarantee the stability of the rock mass; however, continuous excavation of the slope fully, redistributed the rock mass internal stress, and gradually increased deformation. Consequently, the gradually accumulated stress on the ordinary anchor cables exceeded their bearing capacity and ultimately led to anchor cable failure and local collapse of the slope (Fig. 15a). In contrast, NPR anchor cables can undergo axial tension along with large-scale rock mass deformation, absorb the energy produced by slow deformation, maintain constant resistance, accommodate a high degree of deformation, avoid anchor cable tensile failure due to the effects of large-scale rock mass deformation, and drive the slope towards a secondary equilibrium. The side of the model supported by NPR anchor cables had fewer fractures and was more stable.

Bending and fracturing was observed in the middle area between the two anchor cables types. After failure of the ordinary anchor cables, the rock mass on the ordinary anchor cable side of the slope has no anchoring force to resist the stress adjustment inside the slope. As a result, fracturing occurred along the relatively weak joints between the rock mass on the ordinary anchor cable-supported side and that on NPR anchor cable-supported side, and the slope experienced local collapse on the ordinary anchor cable-supported side. When slope excavation was finally finished, the slope was stable on the NPR anchor cable-supported

side, which would allow for normal mining work in the mining area; however, the local instability collapse on the ordinary anchor cable-supported side would pose a threat to mining work (Fig. 15b).

6. Conclusions

Through investigating the field failure characteristics of an anti-inclined slope and conducting an indoor physical model experiment, this paper probes the mechanisms by which NPR anchor cable governs the instability failure of anti-inclined slopes.

(1) By analyzing the field instability characteristics of anti-inclined slopes, this paper examines the laws governing the flexural topping deformation of a rock mass of stratified anti-inclined slopes, investigates the mode and characteristics of toppling failure, and increases our understanding of the associated toppling deformation failure mechanisms.

(2) Taking the results of existing studies regarding the extraordinary mechanical properties of engineering-scale NPR anchor cable as a theoretical basis, the study develops a model-scale NPR anchor cable using similarity theory and then uses a tensile testing machine to conduct a static stretching test on model-scale NPR anchor cable. The model-scale NPR anchor cable developed has a constant resistance value ranging from 58 N to 67 N and a constant resistance deformation amount of 6.5 cm. The mechanical properties of the model-scale NPR anchor cable conform to the constant-resistance mechanical properties of engineering-scale NPR anchor cable. Through a physical model experiment reinforced by model-scale NPR anchor cable, the study determines the stress evolution laws of NPR anchor cable during slope excavation, proving that NPR anchor cable can be used to monitor the sliding force in an anti-inclined slope throughout excavation, which lays the foundation for the application of NPR anchor cable monitoring technology to the advanced warning of anti-inclined slope failure.

(3) Relying on a self-developed "plasterboard-based experimental system to model an engineering disaster," this study builds a generalized geological model and performs a physical model experiment-based study to explore the mechanism of stratified anti-inclined slope reinforcement using model-scale NPR and ordinary anchor cables. The physical model is monitored using static strain data acquisition equipment, an infrared thermal imager, tension sensors, and DSCM displacement field measurement equipment. The evolution of the displacement field, strain field, temperature field, and anchor cable force are determined during excavation of the physical model. By comparing the evolutionary characteristics with images from both the instability failure test of the anti-inclined slope model and the deformation characteristics on the two sides of the slope, which are reinforced by different types of anchor cables, the mechanisms by which NPR anchor cable governs the instability failure of anti-inclined slopes during excavation are determined.

(4) Relative to ordinary anchor cables, NPR anchor cables can undergo axial tension along with large-scale rock mass deformation, absorb the energy produced by slow deformation through the friction between their constant-resistance body and constant-resistance casing, maintain constant resistance, accommodate a large amount of deformation, control the stability of the slope under the combined action of the supporting body-rock mass, avoid tensile failure due to major deformation of the rock mass, drive the rock mass towards a new mechanical equilibrium, and have a more significant economic benefit. NPR anchor cables can also break through the bottleneck imposed by traditional small-deformation materials (i.e., tensile failure due to a failure to resist the large-scale toppling deformation of anti-inclined slopes), and offer a new measure for controlling the instability of anti-inclined slopes.

Declaration of competing interest

No conflict of interest exits in the submission of this manuscript, and the manuscript is approved by all authors for publication. I would like to declare on behalf of my co-authors that the work described is original research that has not been published previously.

Acknowledgements

This work was supported by the the National Natural Science Foundation of China (NSFC) (41941018) and the Fundamental Research Funds for the Central Universities of China (B210201001).

References

1 Tang HM. *Fundamentals of Engineering Geology*. Beijing: Chemical Industry Press; 2008.
2 Talobra J. *La mecanique des rockes appliquée aux travaux publics*. Paris: Dunod; 1957.
3 Freitas DMH, Watters RJ. Some field examples of toppling failure. *Geotechnique*. 1973;23(4):495–514.
4 Goodman RE, Bray JW. Toppling of rock slopes. In: *Proceedings of ASCE Specialty Conference, Rock Engineering for Foundations and Slopes. Colorado: Boulder*. 1976: 201–234.
5 Aydan O, Kawamoto T. The stability of slopes and underground openings against flexural toppling and their stabilisation. *Rock Mech Rock Eng*. 1992;25(3):143–165.
6 Lu ZZ. *Principles of Engineering Geology*. Beijing: China Water Resources and Hydropower Press; 2001.
7 Qi SW, Wu FQ, Yan FZ, Lan HX. Mechanism of deep cracks in the left bank slope of Jinping first stage hydropower station. *Eng Geol*. 2004;73(1-2):129–144.
8 Amini M, Ardestani A. Stability analysis of the north-eastern slope of Daralou copper open pit mine against a secondary toppling failure. *Eng Geol*. 2019;249:89–101.
9 Adhikary DP, Dyskin AV. Modelling of progressive and instantaneous failures of foliated rock slopes. *Rock Mech Rock Eng*. 2007;40(4):349–362.
10 Tu XB, Dai FH, Lu XJ, Zhong HY. Toppling and stabilization of the intake slope for the Fengtan Hydropower Station enlargement project, Mid-South China. *Eng Geol*. 2007;91(2-4):152–167.
11 Amini M, Sarfaraz H, Esmaeili K. Stability analysis of slopes with a potential of slide-head-toppling failure. *Int J Rock Mech Min Sci*. 2018;112:108–121.
12 Zhang GC, Wang F, Zhang H, Tang HM, Li XH, Zhong Y. New stability calculation method for rock slopes subject to flexural toppling failure. *Int J Rock Mech Min Sci*. 2018;106:319–328.
13 Garcia-Moya SA, Gonzalez-Galindo J, Olalla C. Underdip toppling failure mechanism: case study retrospective analysis and its most determinant parameters. *Int. J. Geomechan*. 2019;19(6):1–13.
14 Li LQ, Ju NP, Zhang S, Deng XX, Sheng DC. Seismic wave propagation characteristic and its effects on the failure of steep jointed anti-dip rock slope. *Landslides*. 2019;16 (1):105–123.
15 Evans RS. Analysis of secondary toppling rock failures-the stress redistribution method. *Q J Eng Geol Hydrogeol*. 1981;14(2):77–86.
16 Teme SC, West TR. Some secondary toppling failure mechanisms in discontinuous rock slope. In: *Proceedings of 24th US Symposium on Rock Mechanics, College Station, Texas*. 20-23 June 1983:193–204.
17 Liu CH, Jaksa MB, Meyers AG. Improved analytical solution for toppling stability analysis of rock slopes. *Int J Rock Mech Min Sci*. 2008;45(8):1361–1372.
18 Guo SF, Qi SW, Yang GX, Zhang SS, Saroglou C. An analytical solution for block toppling failure of rock slopes during an earthquake. *Appl Sci*. 2017;7(10):1008.
19 Leon-Buendia C, Santamaria-Arias J, Alejano LR. *Analysis of a Complex Slope Failure in a Quartzite Slope*. Vigo, Spain: Taylor & Francis-Balkema; 2014.
20 Yang XB, Huang RQ, Shen JH, Cao YJ. Characteristics and mechanism of slope deformation at intake of flood-discharge tunnel No.2 of zipinpu hydropower station. *Chin J Rock Mech Eng*. 2005;24(12):2035–2040.
21 Zheng Y, Chen XY, Liu TT, Zhang HN, Xia KZ, Liu F. Study on the mechanisms of flexural toppling failure in anti-inclined rock slopes using numerical and limit equilibrium models. *Eng Geol*. 2018;237:116–128.
22 Li Z, Wang JA, Li L, Wang LX, Liang RY. A case study integrating numerical simulation and GB-InSAR monitoring to analyze flexural toppling of an anti-dip slope in Fushun open pit. *Eng Geol*. 2015;197:20–32.
23 Majdi A, Aydan O, Amini M. New physical modeling of flexural toppling failure with titling machine. In: *Proceedings of the 12th ISRM International Congress on Rock Mechanics. Beijing*. October 2012:798–799.
24 Nishimura T, Nakamura K, Kohno M, et al. *A Small Scale Laboratory Test Using Shaking Table Apparatus for Toppling Failure of Rock Slopes*. Lausanne, Switzerland: Taylo & Francis-Balkema; 2013.
25 Ueda H, Nishimura T, Nakamura K, et al. *A Small Laboratory Test and Discontinuous Modeling Using DEM on Flexural Toppling Failure of Rock Slopes*. Fukuoka, Japan: CRC Press/Balkema; 2013.
26 Chen CX, Zheng Y, Sun CY. An analytical approach on flexural toppling failure of counter-tilt slopes of layered rock. *Chin J Rock Mech Eng*. 2016;35(11):2174–2187.

27 Huang RQ, Zhao JJ, Ju NP, Li G, Lee ML, Li YR. Analysis of an anti-dip landslide triggered by the 2008 Wenchuan earthquake in China. *Nat Hazards*. 2013;68(2):1021–1039.
28 Li LQ, Ju NP, Zhang S, Deng XX. Shaking table test to assess seismic response differences between steep bedding and toppling rock slopes. *Bull Eng Geol Environ*. 2019;78(1):519–531.
29 He MC, Wang Y, Tao Z. A new early-warning prediction system for monitoring shear force of fault plane in the active fault. *J. Rock Mech. Geotech. Eng.* 2010;2(3):223–231.
30 Tao ZG, Zhu C, Zheng XH, Pang SH, He MC. Slope stability evaluation and monitoring of Tonglushan ancient copper mine relics. *Adv Mech Eng*. 2018;10(8):1–16.
31 Tao ZG, Zhang HJ, Zhu C, Hao ZL, Zhang XL, He MC. Design and operation of App-based intelligent landslide monitoring system: the case of three gorges reservoir region. *Geomatics, Nat Hazards Risk*. 2019;10(1):1209–1226.
32 Tao Z, Wang Y, Zhu C, Xu HX, Li G, He MC. Mechanical evolution of constant resistance and large deformation anchor cables and their application in landslide monitoring. *Bull Eng Geol Environ*. 2019;78:4787–4803.
33 Zhu C, Pang SH, Zhao JZ, Tao ZG, Han WS, Yin XH. Analysis of slope deformation caused by subsidence of goaf on Tonglushan ancient mine relics. *Geotech Geol Eng*. 2019;37(4):3435–3446.
34 Tao ZG, Zhu C, Zheng XH, Wang DS, Liu YP, He MC. Failure mechanisms of soft rock roadways in steeply inclined layered rock formations. *Geomatics, Nat Hazards Risk*. 2018;9(1):1186–1206.
36 He MC, Gong WL, Wang J, et al. Development of a novel energy-absorbing bolt with extraordinarily large elongation and constant resistance. *Int J Rock Mech Min Sci*. 2014;67(67):29–42.
37 He MC, Chen Li, Gong Weili, Li SL. Dynamic tests for a constant-resistance-large-deformation bolt using a modified SHTB system. *Tunn Undergr Space Technol*. 2017;64:103–116.
38 Sun XM, Zhang Y, Wang D, Yang J, Xu HC, He MC. Mechanical properties and supporting effect of NPR bolts under static pull test conditions. *Int. J. Min Met. Mater*. 2017;24(1):1–9.
39 Zhu C, Zhang K, Cai H, Tao ZG, An B, He MC. Combined application of optical fibers and NPR bolts to monitor deformation of a pit-in-pit foundation. *Adv Civ Eng*. 2019;2019(1):1–16.
40 Zhu C, He MC, Karakus M, Cui XB, Tao ZG. Investigating toppling failure mechanism of anti-dip layered slope due to excavation by physical modelling. *Rock Mech Rock Eng*. 2020. https://doi.org/10.1007/s00603-020-02207-y.